Journal of Materials Chemistry C

Accepted Manuscript

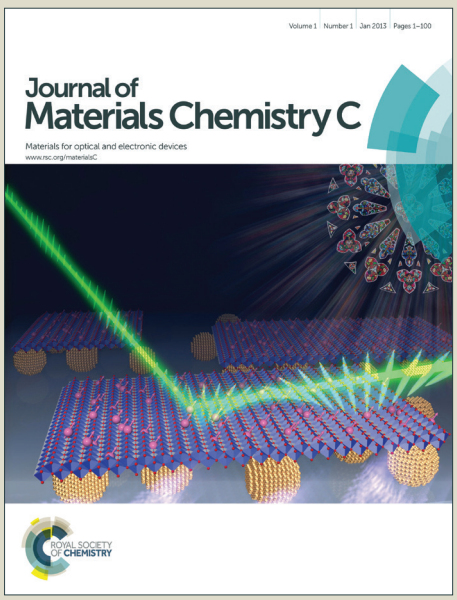

ROYAL SOCIETY OF CHEMISTRY

www.rsc.org/materialsC

Magnetic Macro-Initiators

K. R. Miller and M. D. Soucek
Department of Polymer Engineering
University of Akron, Akron OH 44325

Abstract

Macro-initiators were prepared using three magnetic nanoparticles, Fe_3O_4, FeCo, or Co. Azo free radical initiators were grafted onto the magnetic particles in a two-step reaction utilizing alkoxysilane and ambient temperature esterification reactions. The magnetic initiators (MI) were characterized using IR, DSC, TGA, SEM with EDAX, and DLS. Alternating gradient magnetometer gave saturation magnetization (Ms) values of 42.1, 178.3, and 36.1 Am_2/kg for Fe_3O_4, FeCo, and Co MIs respectively. Bulk polymerization of styrene was used to assess the effectiveness of MIs in free radical polymerization. Molecular dynamic (MD) simulations were performed on the magnetic macro initiators to determine the feasibility of initiating free radical polymerization via the application to an externally applied AC MF. The MD simulations showed magnetically induced polymerization is possible with a minimum force of 62 kcal/mol·Å required to be applied to the core of the MI in order to decompose the C-N bond of the azo group, producing free radicals.

Introduction

Magnetic nanoparticles (MNs) are interesting because the magnetic properties they display are much different than that of the bulk material[1]. MNs have a great potential to be used in applications such as magnetic ferro-fluids[2], contrast agents for imaging[3], biomedical applications[4], and drug delivery[5]. However, due to MN dipole-dipole attractions, MNs tend to aggregate. To help prevent aggregation, polymeric stabilizers are usually grafted onto the surface of the MNs. Hindering particle aggregation is important to preserve the magnetic properties of the particles as well as permitting a good dispersion of the particles to be obtained[6].

Polymers can be anchored to the surface of nanoparticles by: 1)Physisorption - weak bond is formed between the particle surface and the polymer; 2) Grating to technique - polymer end-group reacts with the particle surface; 3) Grafting from technique - the growth of polymer chains from one end of the chain initiator anchored to the particle surface through chemisorption. Out of these three methods, the grafting from technique gives the highest grafting density because polymer chains are grown from small molecules reacting with the surface of the MN and the tethered polymer chains are forced to stretch away from the surface[7].

In using the "grafting from" method, macro-initiators (MIs) are produced for the grafting of initiators onto the surface of the MNs. Atom transfer radical polymerization (ATRP) initiators are commonly used because narrow polydispersed polymers can be obtained with relatively low radical concentration[7-8]. Anchoring moieties that have been used to graft ATRP initiators to magnetic nanoparticles include, but are not limited to: phosphonate ($-PH(OH)_2$) [7, 9], chlorosilane ($-SiCl_3$)[8], carboxylic acid group (-COOH)[10]. In

addition, peroxide based[11] and azo compounds[12] have been grafted onto MNs in order to create a polymer shell via the polymerization of vinyl monomers.

In the production of magnetic macro-initiators, magnetite has almost exclusively been used as the magnetic core, limiting the magnetic properties that can be achieved by use of different magnetic cores. In addition, the synthesis of magnetic MIs has mainly focused on the production of a polymer shell surrounding the MI[7, 12-13]. Based on the available literature, it is essential to produce magnetic macro-initiators that possess different magnetic properties such that the particles can be matched to an end application. Furthermore, the production of stable magnetic MIs that are capable of forming networks within a polymeric system during polymerization would be beneficial in order to impart magnetic properties into non-magnetic polymer materials.

Previous work on magnetically cured systems have all focused on the generation of thermal heat throughout the bulk of an adhesive or composite via vibration of magnetic nanoparticles contained in the material. Heat is generated internally by means of vibrating magnetic particles embedded in the adhesive. The vibrations arise due to the application of an AC MF. When the field is on, the magnetic particles align themselves parallel to the applied MF and then reorganize into a disordered state once the field is switched off. The vibrations of the magnetic particles allow heat to be built up using a high frequency[14]. The drawback of this curing method is that since a large amount of heat is generated the substrate cannot be heat sensitive. This study is focusing on initiation of free radicals via the vibration of magnet MIs without the generation of deleterious heat.

In this work, magnetic macro-initiators are synthesized by grafting an azo-initiator onto the surface of (3-aminopropyl)triethoxysilane (APTS) coated MNs. To obtain different magnetic properties Fe_3O_4, FeCo, or Co MNs will be used as cores. For each of the macro-initiators, the grafting density, particle stability, and magnetic properties will be investigated. In addition, the bulk polymerization of polystyrene will be performed in order to evaluate the free radical polymerization ability of the magnetic MIs. To determine the ability of the MIs to initiate free radical polymerization via the application of an external AC magnetic field, molecular dynamics (MD) simulations and will be performed. In the MD simulation, force will be applied to the magnetic MI at ambient conditions to determine if it is possible to break the attached weak link through transfer of energy.

Experimental

Materials

Iron(II) sulfate heptahydrate, iron(III) chloride hexahydrate, ammonim hydroside solution 28% (w/w), cobalt(II) chloride hexahydrate, Sodium borohydride, (3-aminopropyl)triethoxysilane (APTS), citric acid monohydrate, ethanol (200 proof), potassium phosphate monobasic ≥98%, sodium chloride, hydrochloric acid, N-(3-Dimethylaminopropyl)-N'-ethylcarbodiimide hydrochloride ≥98.0%, 4,4'Azobis(4-cyanovaleric acid) ≥98.0% (ACV), phosphate buffered saline (PBS), methylene chloride, and styrene were purchased form Sigma and used without further purification.

Synthesis of APTS coated magnetite nanoparticles

Magnetite nanoparticles were synthesized by a co-precipitation method. In a 100 mL three neck flask equipped with a mechanical stirrer were taken 0.675 mmol $FeSO_4 \cdot 7H_2O$ and 1.35 mmol $FeCl_3 \cdot 6H_2O$ in 40 mL of deionized water. The mixture was stirred under nitrogen gas for 30 min. Magnetite nanoparticles were obtained by adding 12 mL 28% (w/w) NH_4OH to the solution, immediately following addition of NH_4OH a black precipitate formed. Solution vigorously stirred under nitrogen for an additional 30 min. Next 0.9 mL APTS was added over a 10 min time period, followed by further stirring under nitrogen for 30 min. Particles were washed 5 times with deionized water by using magnetic separation.

Synthesis of APTS coated FeCo nanoparticles

FeCo nanoparticles were prepared by co-precipitation, method. To a 500 mL three necked flask equipped with a magnetic stirrer, 1.0 mmol $FeCl_3 \cdot 6H_2O$ and 1 mmol $CoCl_2 \cdot 6H_2O$ were added with 150 mL deionized water. Mixture stirred for 30 min under nitrogen. 1 mmol $NaBH_4$ dissolved in 50 mL deionized water was added to the solution followed by stirring under nitrogen for 4 h. Next 2 mL of APTS was added and the mixture was stirred for 1 h under nitrogen. The particles were washed with deionized water 5 times to remove residual Na and Cl ions using magnetic separation.

Synthesis of APTS coated Cobalt nanoparticles

Cobalt nanoparticles were synthesized by the reduction of Co^{2+}. To a 1 L three neck round bottom flask equipped with a magnetic stirrer and containing 100 mL deionized water were added 10 mmol $NaBH_4$ and 0.005 mmol citric acid monohydrate. Solution was stirred under nitrogen for 30 min. Next, 1 mmol $CoCl_2 \cdot 6H_2O$ dissolved in

0.2 mL deionized water was added to the mixture; black precipitate immediately formed upon addition of the cobalt solution. Following 1 min of stirring, 500 mL of an ethanolic solution containing 350 μL APTS was added. After 15 min of stirring under nitrogen the particles were washed 5 times with ethanol by using magnetic separation.

Synthesis of Magnetic Macro-initiators

Magnetic macro-initiators were synthesized by a coupling reaction with 4,4' azobis(cyanovalericacid acid) (ACV). The APTS coated MNs (Fe3O4, FeCo, or Co) were activated by sonication for 30 min in 20 mL of coupling buffer. Coupling buffer was a 0.01 M potassium phosphate, 0.15 M sodium chloride solution adjusted to pH 5.6 with hydrochloric acid. The MNs were then magnetically separated and resuspended in 4 mL of the coupling buffer. Next, 10 mL of a solution containing 8.6 mmol of N-(3-Dimethylaminopropyl)-N'-ethylcarbodiimide hydrochloride and 8.6 mmol of ACV in deionized water was added to the MNs suspension. Reaction mixture was shaken for 24 h at room temperature in the absence of light. Magnetic macro-initiators were then magnetically separated and washed 3 times with distilled H_2O using magnetic separation.

Characterization

FTIR spectra were measured on a Nicolet-380 spectrometer in the range of 4000 to 400 cm^{-1}. Absorbance spectra were acquired at 4 cm^{-1} resolution and the signal was averaged over 32 scans. Samples were prepared by mixing a small amount of the dried MIs (1-5 mg) with dry KBR powder. The sample mixture was then pressed together with a bolt press to form a transparent disk.

Differential scanning calorimetry (DSC) traces were recorded on a TA instrument DSC Q200 model. All the samples were heated from -30 to 150 °C at a heating rate 5 °C·min^{-1} under nitrogen atmosphere.

Thermogravimetric analysis (TGA) of the MIs was performed on a TA instrument TGA Q500 model. Samples were heated form 30 to 650 °C in air with a scan rate of 10 °C · min^{-1}.

Dynamic light scattering (DLS) was used to quantify the hydrodynamic diameters and particle size distribution of the MIs. Samples were prepared by suspending 1 mg of the MIs in 10 mL of deionized water. A 90Plus Brookhaven DLS spectrophotometer equipped with a BI9000 correlator and a 30 mW red diode laser operating at 673 nm was used for the scattering experiments that were performed at room temperature, and the scattering intensity was recorded at 90°. The data was processed using multimodal size distribution analysis based on non-negatively constrained least squares. Each measurement was performed 5 times, 2 min per measurement, with the mean and standard deviation reported.

Scanning electron microscopy (SEM) (Hitachi S2150) was used to qualitatively evaluate the size and shape of the MIs. The SEM samples were prepared by suspending 1 mg of MIs in 10 mL of ethanol. Solution was dropped onto a stub and allowed to dry.

Stability of Magnetic Macro-initiators in PBS solution

The stability of the MIs was determined by monitoring the change in hydrodynamic diameter of the particles via DLS. Samples were prepared by suspending 1

mg of the MIs in 20 mL of a PBS solution, pH 7.4. DLS measurements were recorded over a period of 10 days. Each measurement was preformed 5 times, 2 min per measurement, with the mean and standard deviation reported.

Magnetic Properties

Magnetization curves at room temperature for the MIs were obtained on a Princeton Micromag 2900 alternating gradient magnetometer. Dried powder samples were suspended in glass capillary tubes (1.5 mm OD x 4 mm long). Samples ran in triplicate, with the mean and standard deviation reported.

Polymerization of Styrene with Magnetic Macro-initiators

Into a polymerization vial, magnetic macro-initiators and 5 g (0.048 mol) of styrene monomer were charged. Polymerization was carried out by immersing the vial in oil bath at 80 ℃ for 5 hr. In addition, polymerization initiated by 2 wt. % (0.36mmol) ACV was performed. The amount of magnetic macro-initiator added was determined from the grafting density such that the molar amount of ACV was constant for all reactions.

The residual monomer content was determined by gas chromatography (GC) analysis. The unreacted monomer was extracted by adding 2 mL of methylene chloride to the polymerized styrene and shaking for 1 hr. Next, a 1 μL aliquot was injected into a Varian CP-3800 gas chromatograph equipped with a VF-5 fused silica capillary column (30 m × 0.25 i.d. mm, 0.25 μm film thickness, Varian, USA). The optimum column separation was obtained with an initial temperature of 100 °C and a ramp rate of 5

°C/min to 150 °C, followed by a ramp rate of 25 °C/min to reach the final temperature. The final temperature was set to 200 °C, which was held for 5 min so that all the components eluted out of the column. The carrier gas was hydrogen. Concentration was determined by comparing the area of the styrene peak to external standards. Styrene concentrations used for external standards include: 1, 2, 4, and 6 M. Conversion of the polymerized styrene was calculated according to Equation 1:

$$Conversion\ (\%) = \frac{M_T - M_R}{M_T} \times 100 \quad (1)$$

where M_T is the total amount of monomer added and M_R is the residual amount of monomer present after polymerization.

Calorimetric Study of Magnetic particles with and without Grafted with Azo-Initiator

Calorimetry traces of the magnetic MIs under the influence of an AC MF were obtained by measuring the change in temperature of an MI solution. To determine the exotherm resulting for the decomposition of the azo group of the magnetic MI due to the application of an AC MF, the temperature change was monitored as a function of time during exposure to an externally applied MF. Temperature change was monitored for both a water/MI solution and that of a water/pre-azo grafted magnetic particle (silica coated magnetic particle). The heat flow was determined according to equation 2[15],

$$\boldsymbol{q = mC_p\Delta T} \quad (2)$$

where m is the mass of solution, Cp is the specific heat capacity of the solution (in this case that of water), and delta ΔT is the temperature difference between the water/MI solution and the water/pre-azo grafted magnetic particle solution. The temperature

difference between the pre-azo grafted and azo grafted magnetic particles permits for the determination of the temperature increase resulting for the decomposition of the azo group as opposed to the temperature increase resulting from power dissipation of magnetic particles in an AC MF[16].

In a 10 mL glass vial, 0.1 g of MIs were suspended in 2 mL of deionized water, creating a 5 wt. % solution. The glass vial was then place in an insulated holder surrounded by an electromagnetic coil. An IR temperature sensor was placed over the top of the vial to measure the temperature change of the solution during application of an AC MF. Scheme 1 shows a depiction of the instrument setup. The AC MF was applied for up to 3 min, during which the temperature was continuously monitored. The AC MF for this experiment and all subsequent experiments was supplied by an circular copper coil (50 mm ID, 5 turns) attached to a RF generator (MSI automation, USA) operating a fixed frequency of 480 kHz and a 12kA/m magnetic field. The same procedure was repeated for each of the MIs and their respective pre-azo grafted magnetic particles. The obtained temperature readings were then used in conjunction with Equation 2 to determine the heat flow for each of the magnetic MIs.

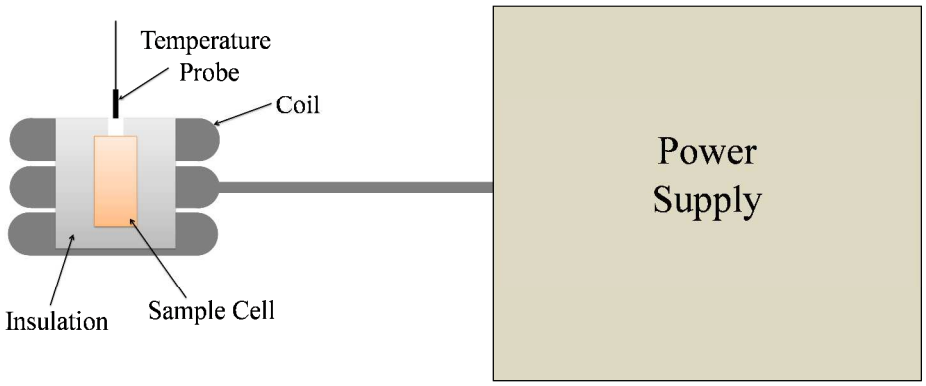

Scheme 1: Calorimetric Set-up for In situ heat flow measurement within an Oscillating Magnetic field

Model Construction for Feasibility of Magnetic Polymerization

To understand the cleavage process of the azo bond contained in the MI under the influence of a magnetic field, we present a simple molecular model which follows the experimental process of bond breaking. To achieve azo bond cleavage, we just consider the magnetic field influence on the magnetic core without application of any additional thermal energy to the system. The system was simplified to include one azo group which consists of a single azo initiator molecule grafted with an APTS molecule in the aqueous media. Figure 1 shows the single molecule which was grafted onto the magnetic core.

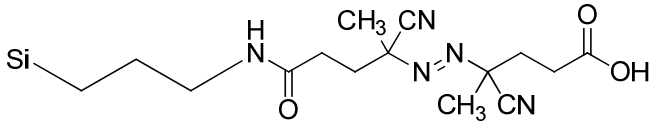

Figure 1. ATPS-AZO molecule used in simulation

In order to calculate the minimum magnetic force required to break the azo bond, molecular dynamics (MD) simulations were performed. First, a molecular model of the detached APTS-AZO molecule in the aqueous media, Figure 2, was constructed with help of Material Studio graphical interface. The main idea behind modeling the detached

APTS-AZO molecule is to understand the breaking of the azo bond. From the experiment, the mechanism of azo bond breaking is due to the exertion of force on the silicon atom from the magnetic core. This force then travels through the grafted APTS-AZO molecule and is responsible for breaking the weak azo bond. In the MD simulation, a force will be applied to the silicon atom which will mimic the process of force exertion by a magnetic field. We use a simulation box size of 2.5 x 4 x 3 nm^3 which contains 978 water molecules, giving a density of 1 g/cm^3.

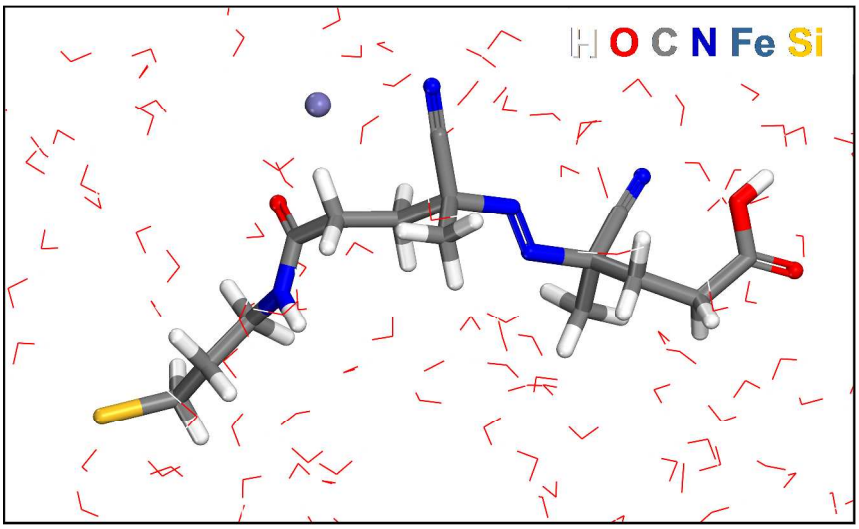

Figure 2. Molecular model of a detached APTS-AZO molecule in the aqueous media

Force Field Parameters and Energy Expression

The energy expression for the grafted initiator molecular system has been chosen the same as in organic and biomolecular force fields, PCFF (Polymer Consistent Force Field). The simplified energy expression of PCFF force is described in the Equation 2.

The energy expression includes bonded as well as non-bonded interactions. Bonded interactions consider bond stretching, angle bending, and dihedral angle torsion. Non bonded terms include Coulomb and van der Waals interactions. Details of force field parameters used are listed in the supplementary data, Table A-1. Element identification and force field type for the APTS-AZO molecule are shown in Figure 3.

$$E_{pot} = \sum_{ij\,bonded} K_{r,ij}(r_{ij} - r_{0,ij})^2 + \sum_{ijk\,bonded} K_{\theta,ijk}(\theta_{ijk} - \theta_{0,ijk})^2 + \frac{1}{4\pi\varepsilon_0\varepsilon_r} \sum_{\substack{ij\,nonbonded \\ (1,3\,excl)}} \frac{q_i q_j}{r_{ij}} + \sum_{\substack{ij\,nonbonded \\ (1,3\,excl)}} \varepsilon_{0,ij} \left[2\left(\frac{\sigma_{0,ij}}{\sigma_{ij}}\right)^9 - 3\left(\frac{\sigma_{0,ij}}{\sigma_{ij}}\right)^6 \right] \quad (3)$$

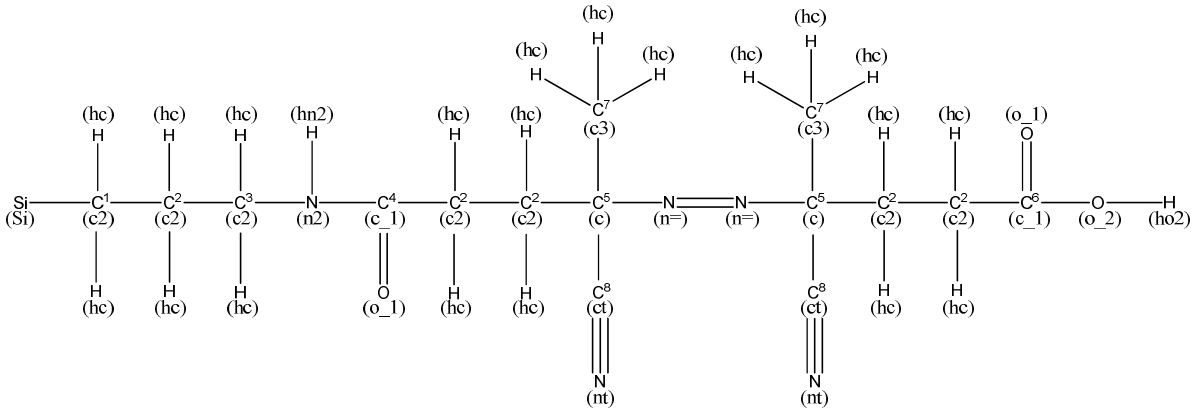

Figure 3. Element identification and force field type for the ATPS-AZO molecule

Simulation Details

The MD simulations were performed using *NVT* ensemble at ambient temperature. The number of particles (N), volume (V), and temperature (T) were kept

constant. At first, the APTS-AZO molecule structure was minimized in the aqueous media using conjugate gradient method by Polak- Ribiere algorithms with the help of Discover program[17]. Therefore, we employed *NVT* dynamics with a time step of 1 fs and temperature control using Andersen thermostat under periodic boundary condition. We fix the spherical cutoff of van der Waals interactions at 1.2 nm. Initially we run the system for 100 ps time for equilibration. Once the system is equilibrated, we use LAMMPS program for the advanced simulation method used for the breaking of azo bond in the aqueous media.

Using the LAMMPS program under NVT ensemble, the system is first equilibrated for 20 ps time with time step of 1 fs. In the next step, an additional force is applied specifically to silicon atom, so that the weakest azo bond can be broken. The amount of force was varied from 30 to 90 kcal/mol-Å with an increment of 5 kcal/mol-Å on the silicon atom. Independent MD runs were performed for each applied force. In the final step of simulations, the bond length between carbon and nitrogen atoms of the azo group were described to be breakable once it reached a maximum defined length (D_{max}) of 2.031 Å[18].

Results and Discussion

Magnetic MIs were produced by grafting an azo-initiator onto silica coated magnetic cores of Fe_3O_4, FeCo, or Co. A silica coating was used in order to help stabilize the magnetic macro-initiators such that upon dispersion in a medium the particles would be stable until use. The different magnetic cores were chosen to produce magnetic macro-initiators with different magnetic properties. The feasibility of magnetically induced

polymerization was investigated thorough MD simulations. The MD simulation was used to determine if the azo bond could be broken through application of force to the magnetic core. In addition, the MD simulation was used to calculate the minimum required force applied to the magnetic core to break the azo bond.

Synthesis and Characterization

Magnetic macro-initiators were prepared by a co-precipitation or reduction route, Scheme 2, and coated with APTS, Scheme 3. The APTS coated magnetic particles were then reacted with ACV in a coupling reaction, Scheme 4, to produce the magnetic MIs. Surface coating of MNs is an essential step in producing particles that have stable particle size and magnetic properties. Stable particles are especially important in the biomedical field, if particles begin to degrade and the MN core is revealed, toxicity issues can arise. Furthermore, if the particles aggregate the magnetic properties will be affected[19].

a) $2Fe^{3+} + Fe^{2+} + 8OH^{-} \rightarrow FeO{\cdot}Fe_2O_3 + 4H_2O$

b) $BH_4^{-} + Fe^{2+} + Co^{2+} + 2H_2O \rightarrow FeCo + BO_2^{-} + 4H^{+} + 2H_2$

c) $2CoCl_2 + 4NaBH_4 + 9H_2O \rightarrow Co_2B + 4NaCl + 12.5H_2 + 3B(OH)_2$

$4Co_2B + 3O_2 \rightarrow 8Co + 2B_2O_3$

Scheme 2: Reactions used in the preparation of a) Fe_3O_4, b) FeCo, and c) Co particles

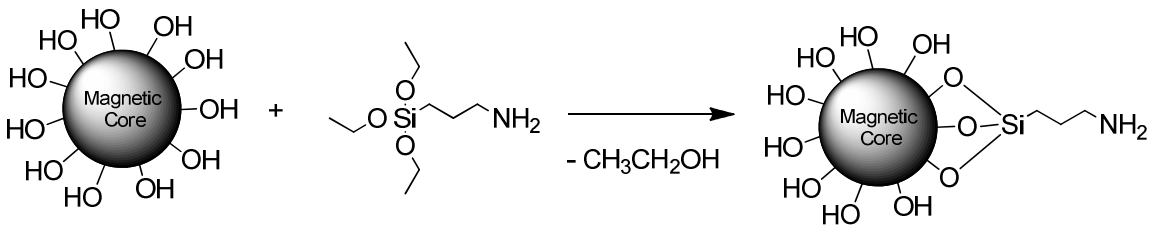

Scheme 3: Coating of magnetic particles with APTS

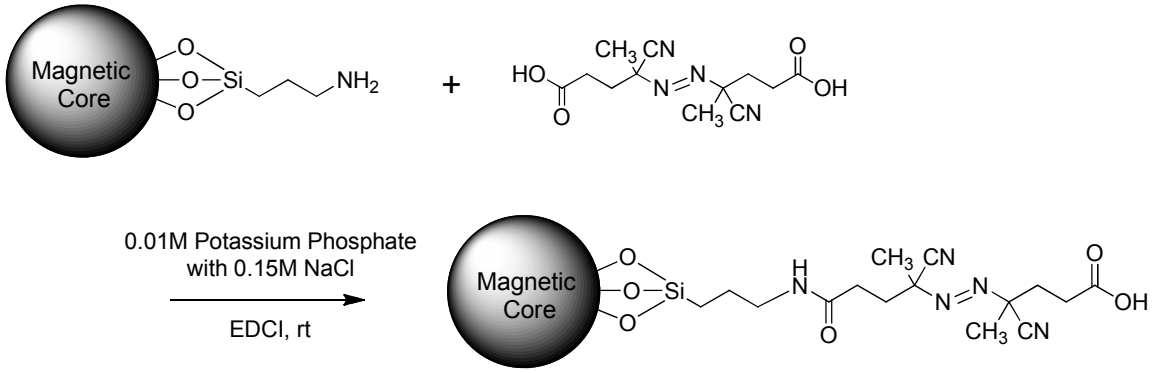

Scheme 4: Synthesis pathway to produce magnetic macro-initiators by grafting ACV onto the APTS coated magnetic particles

Coating of the magnetic particles with APTS and subsequent grafting of ACV onto the particles was investigated with FTIR. Figure 4 shows the FTIR spectra of the APTS coated and ACV grafted Fe_3O_4 particles. The amine terminated nanoparticles had an absorption band at 572 cm^{-1} due to the Fe-O bond. The absorption at 1090 cm^{-1} was assigned to the C-N stretch of a primary amine which overlaps with the Si-O band at 1047 cm^{-1}. The magnetic initiator has absorption bands at 1630, 1652, 1710, and 2242 cm^{-1}, corresponding to N=N azo bond, C=O of amide group, C=O of carboxylic acid group, and cyanide group respectively. The absorption bands for the FeCo and Co particles grafted with ACV are shown in Table 1.

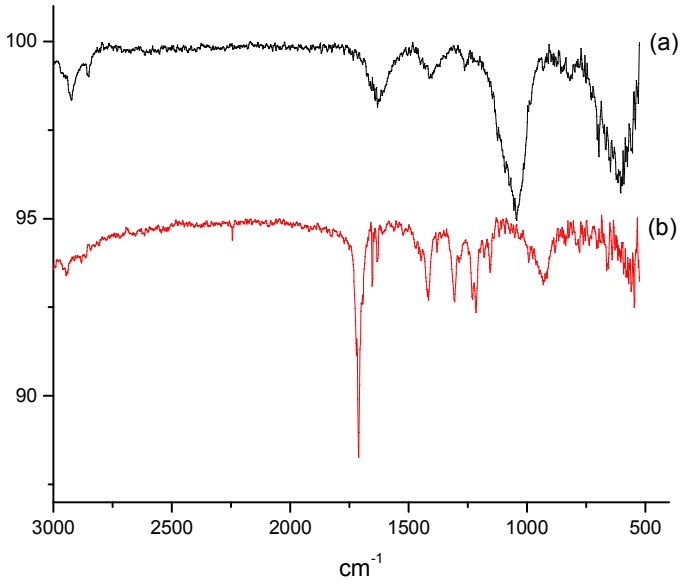

Figure 4: FTIR spectra of a) APTS coated and b) ACV grafted Fe_3O_4 particles

Table 1: FTIR absorption bands for APTs coated, ACV grafted FeCo and Co particles

Wave number (cm^{-1})	Assigned Bond	
	FeCo	Co
575	Fe-O	-
1047	Si-O	Si-O
1650	C=O (amide group)	C=O (amide group)
1710	C=O (carboxylic acid)	C=O (carboxylic acid)
1635	N=N	N=N
2240	CN	CN
2923	C-H	C-H

The MIs were further characterized by EDAX, Figure 5. All the graphs show the presence of silica, oxygen, and carbon. The main use for the EDAX analysis was to observe the metals that are contained in each MI. As expected, Fe_3O_4 MIs displayed a

signal from iron; FeCo MIs produced both iron and cobalt signals, and the Co MIs displayed signals from cobalt. All MIs produced oxygen and silica signals due to APTS surface coating.

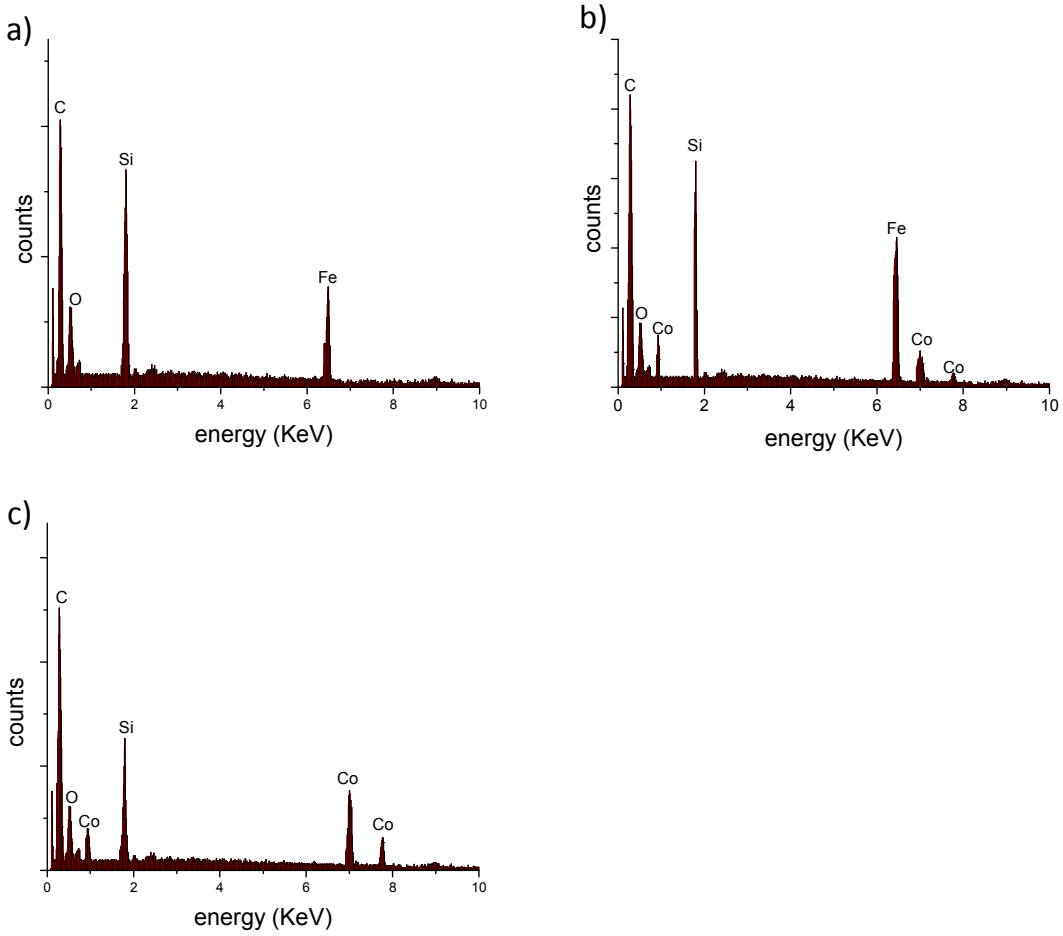

Figure 5: EDAX analysis of a) Fe_3O_4 MI, b) FeCo MI, and c) Co MI

The grafting density of the attached azo initiator was determined by both DSC and TGA. In the DSC measurement, the exothermic decomposition of the azo initiator was monitored. Figure 6 shows the DSC thermograms of the free azo initiator and the Fe_3O_4, FeCo, and Co MIs, respectively. The DSC thermograms confirm that the grafting

did not affect the thermal behavior of the initiator; all exotherm peaks are very close to the same temperature (ca. 126 °C). The grafting density, τ_m, was calculated according to Equation 4:

$$\tau_m = \frac{\Delta H_{exo}^{gi}}{\Delta H_{exo}^{fi} \times M_{fi}} \quad (4)$$

where ΔH_{exo}^{gi} is the enthalpy of decomposition of the grafted initiator ($J \cdot g^{-1}$), ΔH_{exo}^{fi} is the enthalpy of decomposition of the free initiator ($J \cdot g^{-1}$), and M_{fi} is the molecular weight of the free initiator ($g \cdot mol^{-1}$)[20]. Table 2 shows the calculated grafting densities by DSC for the Fe_3O_4, FeCo, and Co MIs.

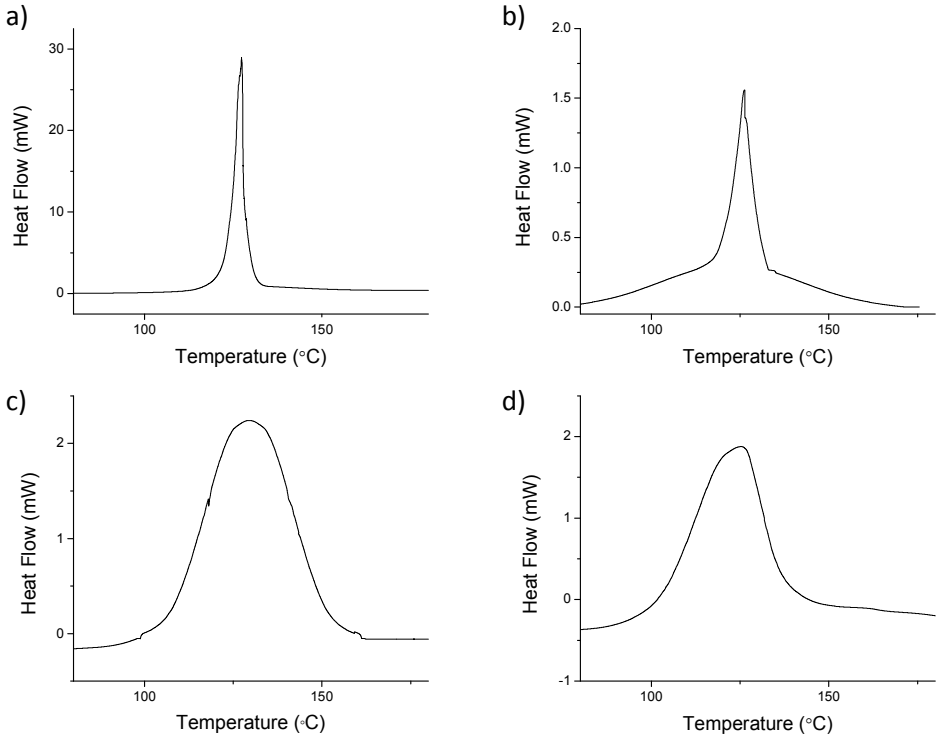

Figure 6: DSC Thermograms: a) free azo initiator, b) Fe_3O_4 MI, c) FeCo MI, and d) Co MI

For the determination of the grafting density by TGA, the weight loss of the APTS coated particles and the azo initiator grafted particles was monitored. Figure 7 shows the TGA thermograms for both the APTS coated particles and the Fe_3O_4, FeCo, and Co MIs. To account for the decomposition of the APTS coating, the final weight loss was determined by subtracting the weight loss of the APTS coated particles from the weight loss of the azo initiator grafted particles. Assuming the difference in weight loss is only from the attached azo initiator, the grafting density can be calculated by use of Equation 5[20b].

$$\tau_m = \frac{\left(\frac{W_{gi}}{100 - W_{gi}}\right) \times 100 - W_S}{M_{fi} \times 100} \quad (5)$$

where W_{gi} is the weight loss of the azo grafted MI, W_S is the weight loss of the APTS coated particle, M_{fi} is the molecular weight of the azo initiator. Table 2 shows the calculated grafting densities from the TGA measurements for the Fe_3O_4, FeCo, and Co MIs. The grafting density results determined by DSC and TGA were similar, with the grafting densities from TGA being 5.6, 6.3, and 23.1 % higher than those calculated by DSC for the Fe_3O_4, FeCo, and Co MIs, respectively.

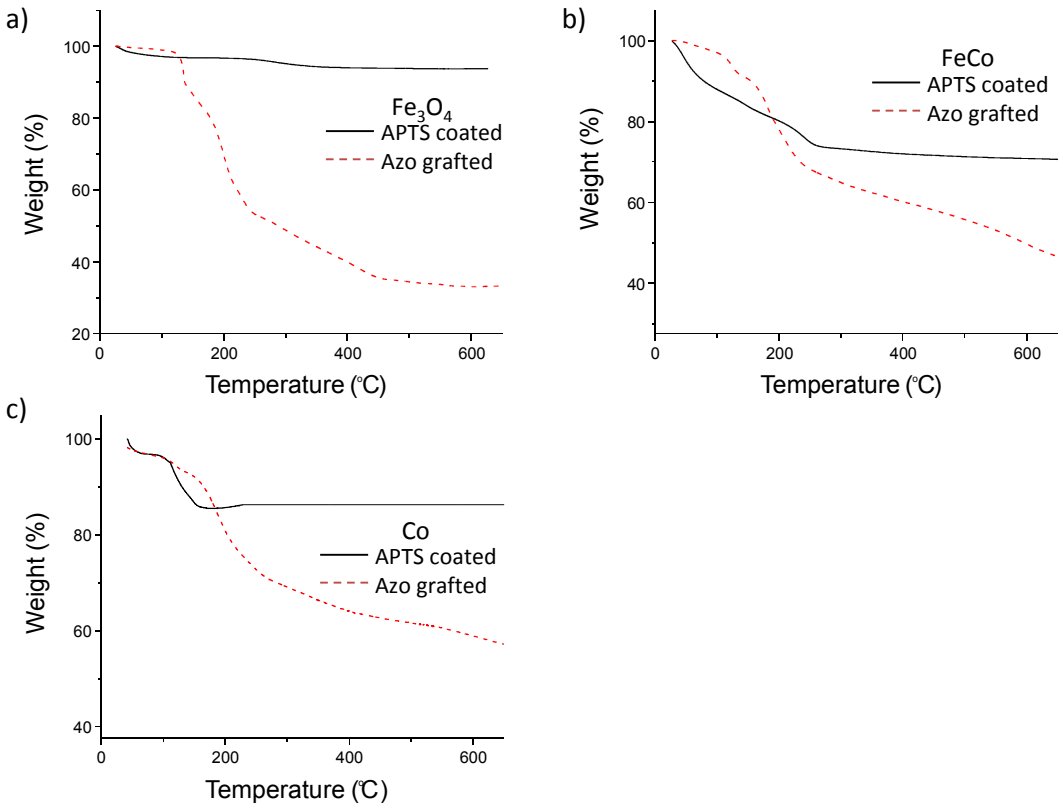

Figure 7: TGA of a) APTS coated(−) and azo grafted Fe_3O_4 particles(--), b) APTS coated(−) and azo grafted FeCo particles(--), and c) APTS coated(−) and azo grafted Co particles(--)

Table 2: Grafting densities of magnetic macro-initiators

Magnetic Core	DSC τ_m x 10^3 (mol/g)	TGA τ_m x 10^3 (mol/g)
Fe_3O_4	1.8	1.9
FeCo	1.6	1.7
Co	1.3	1.6

Particle Size and Stability

Particle size of the MIs was determined by DLS and SEM. The DLS results, Figure 8, showed that the MIs had a diameter of 112 ± 2.7, 164 ± 4.9, and 142 ± 1 nm, for the Fe_3O_4, FeCo, and Co MIs, respectively. SEM images, Figure 9, show the MIs diameters to be ~ 95, 130, and 115 nm for the Fe_3O_4, FeCo, and Co MIs, respectively. As expected, the diameters obtained by DLS are larger than those from the SEM images because DLS measures hydrodynamic diameter. In addition, the SEM images reveal that all the MIs are spherical in shape and have size distributions similar to those obtained by DLS; Co MIs have the least amount of size distribution followed by the Fe_3O_4 and FeCo MIs.

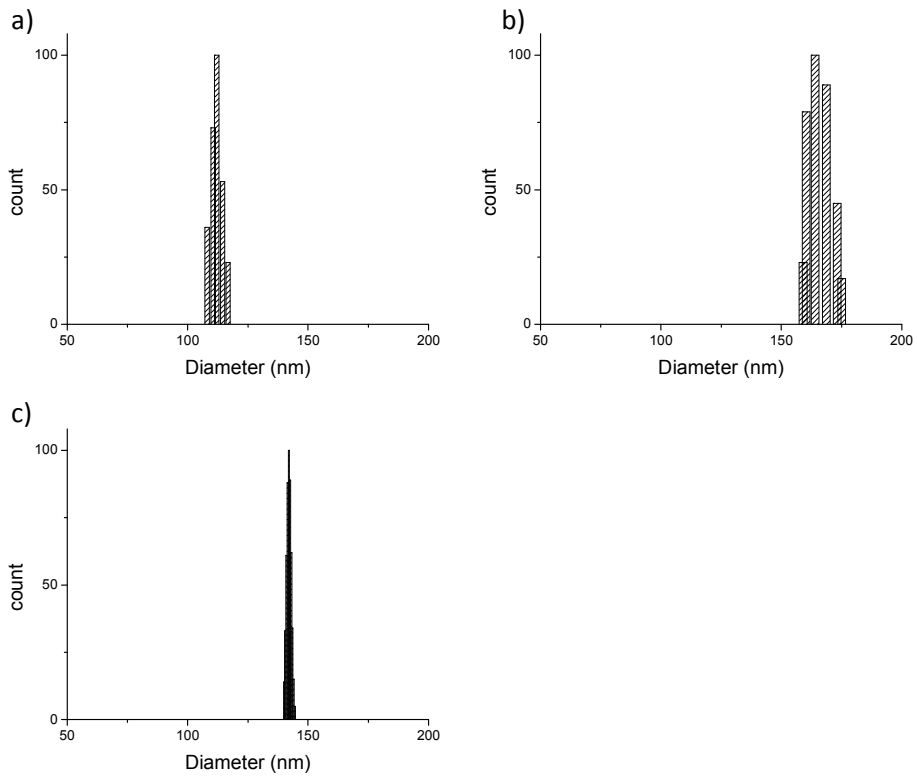

Figure 8: Particle diameter and distribution of a) Fe_3O_4 MIs, b) FeCo MIs, and c) Co MIs

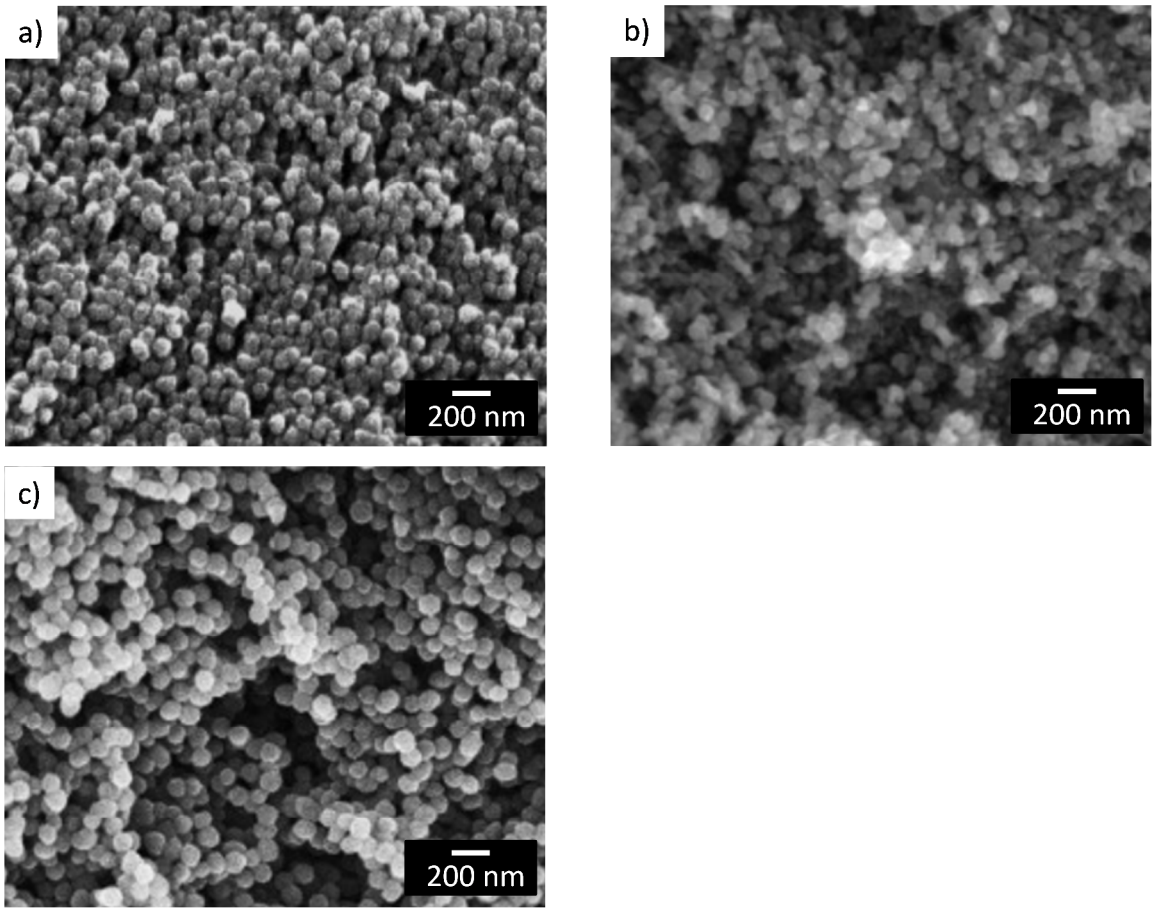

Figure 9: SEM image of a) Fe_3O_4 MIs, b) FeCo MIs, and c) Co MIs

Dynamic light scattering was also employed to evaluate the particle size and aggregation of the MIs in PBS. Figure 10 shows plots of the MIs particle size as a function of time. It is observed that the particle diameter is relatively stable, after 10 days particle size only increased by 7.2, 11.5, and 4.2 % for Fe_3O_4, FeCo, and Co MIs, respectively. The small growth in particles size indicates aggregation is occurring. All the MIs were quite stable with the FeCo MIs showing the largest amount of aggregation, 11.5 % increase in size. Aggregation of the MIs will result in a decrease in initiator efficiency

due the lower distribution of initiating radicals. However, there is no sign of magnetic particle degradation. Degradation would not only result in the loss of magnetic properties[21], but degradation products could be released into the surrounding medium. This could result in lowered performance, and in the case of biomedical applications the degradation products could be potentially hazardous to the patients' health[22].

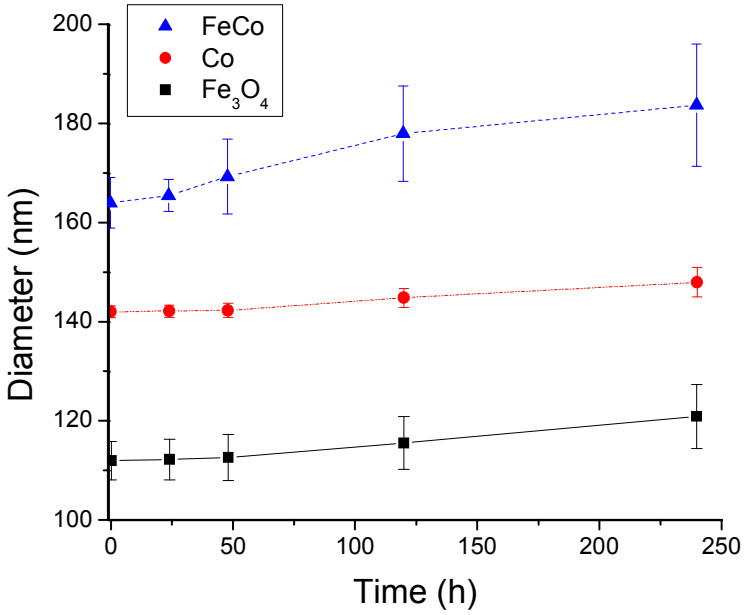

Figure 10: Stability of Fe_3O_4, FeCo, and Co MIs in PBS as a function of time

Magnetic Properties

The magnetic properties of the magnetic MIs were measured by means of an alternating gradient magnetometer. Figure 11 shows the hysteresis curves of each of the three MIs. Both the Fe_3O_4 and Co MIs have an almost closed loop while the FeCo MIs displays a wider loop as compared to the others. From the hysteresis curves, the

saturation magnetization (M_s), remanent magnetization (M_r), magnetic mass susceptibility (χ), and coercivity (H_c) can be determined. Table 3 shows the obtained values for each MI. M_s is the maximum induced magnetic moment that can be achieved in a magnetic field. M_r is the magnetization still present in the material after removal of an external magnetic field. χ relates the magnetization of a material to that of the applied magnetic field ($M = \chi H$); χ is calculated from the initial slope of the magnetization curve. Lastly, H_c is the magnetic field intensity required to lower the magnetization of a material to zero[23].

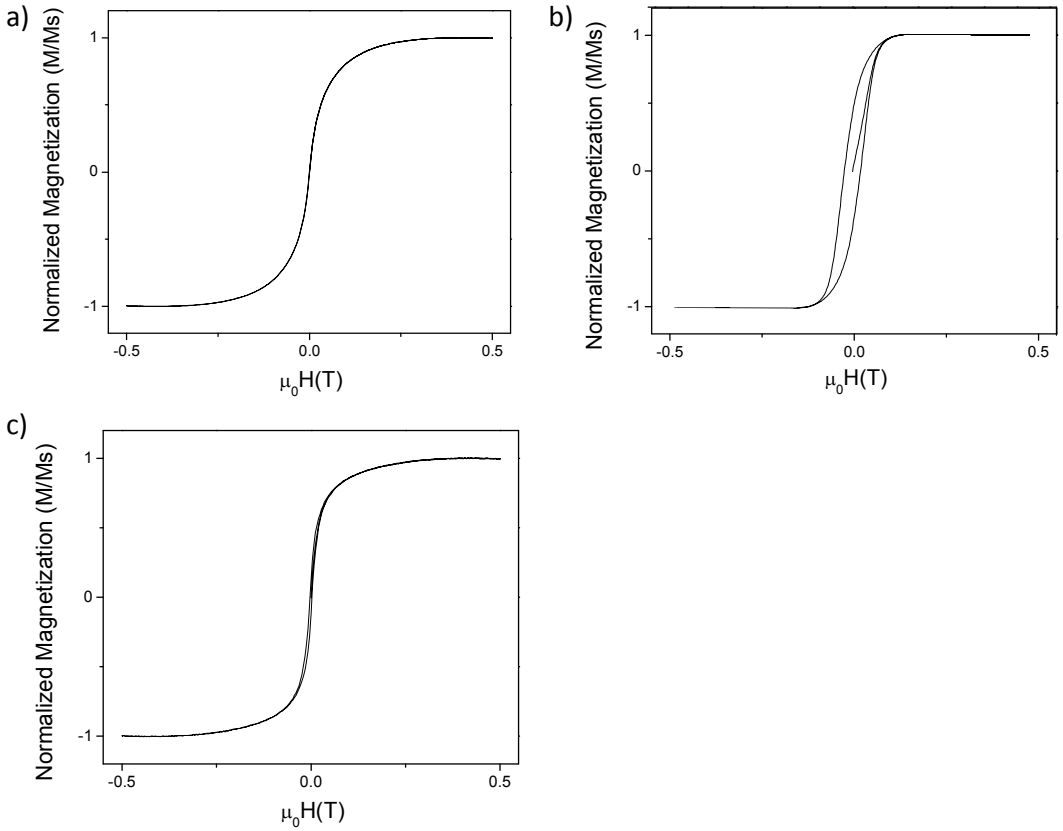

Figure 11: Hysteresis curve for a) Fe_3O_4 MI, b) FeCo MI, and c) Co MI

Table 3: M_s, M_r, χ, H_c values for the MIs

	M_s Am^2/kg	M_r Am^2/kg	X m^3/kg	$\mu_0 H_c$ mT
Fe_3O_4	42.1 ± 2.2	139.1 ± 8.6	465.5 ± 12.1	0.14 ± 5.41
FeCo	178.3 ± 9.2	89.2 ± 7.1	188.5 ± 22.1	49.7 ± 2.2
Co	36.1 ± 7.6	4.34 ± 0.8	345.2 ± 15.4	2.7 ± 0.5

Each of the different MIs has completely reversible hysteresis loops at room temperature. The Fe_3O_4 MIs shows no hysteresis opening, Co MIs have a slight opening, and the FeCo MIs have a fairly large hysteresis opening as compared to the other MIs. For the Fe_3O_4 MI, the M_s was determined to be 42.1 ± 2.2 Am^2/kg, which is much lower than that of bulky Fe (222 Am^2/kg)[24] and other MNs (212 Am^2/kg) [25].The decrease in the M_s of the as prepared Fe_3O_4 MIs may be attributed to the decrease in particle size[26]. As particle size decreases, the magnetization also decreases due to an increase in the volume fraction of oxide on the surface of the particle. The oxide layer is a defect on the MN surface which leads to canted (noncollinear) surface moments, decreasing the M_s[21a]. In addition, the azo-APTS coating can create a diamagnetic layer that contributes as a nonmagnetic mass to the total sample volume[27]. Likewise, small particle size and azo-APTS coating caused the Co MIs to have a lower M_s, 36.1 ± 7.6 Am^2/kg, than that of bulk Co, 170 ± 8 Am^2/kg[28].

The M_s value of the FeCo MIs is 178.3 ± 9.2 Am^2/kg is lower than that of the bulky FeCo counterparts of 220 ± 5 Am^2/kg[28]. As with the Fe_3O_4 MIs, the FeCo MIs can have a lower M_s value than the bulk material due to fine particle size and the azo-APTS

coating. However, due to the larger size of the FeCo MIs as compared to the Fe_3O_4 MIs, the variation between the bulk and FeCo MI M_s is not as large. In addition, FeCo MIs can have a low M_s value due to the existence of boron. In the synthesis of FeCo MNs by the co-precipitation method, two mechanisms can be presented[29], Equations 6 and 7.

$$BH_4^- + Fe^{2+} + Co^{2+} + 2H_2O \rightarrow FeCo + BO_2^- + 4H^+ + 2H_2 \quad (6)$$

$$4BH_4^- + Fe^{2+} + Co^{2+} + 6H_2O \rightarrow FeCoB + 3HBO + 12.5H_2 \quad (7)$$

Therefore, if an excess of boron is used, the content of boron in the FeCo MIs will be higher. As a consequence, the amount of sodium borohydride used in the synthesis of the MIs was reduced to a minimum. The presence of excess boron can also account for the greater size distribution of the FeCo MIs as compared to the Fe_3O_4 and Co MIs.

On the basis of the criteria given by Dunlop[30], single-domain (SD) particles have a M_r/M_s value larger than 0.5, a value between 0.1 and 0.5 for pseudo-single domain (PSD) particles, and a value lower than 0.1 for multi-domain (MD) particles. The Fe_3O_4 and Co MIs display SD behavior with M_r/M_s values of 3.3 and 0.5, respectively. While the FeCo MI displays PSD behavior and has a M_r/M_s value of 0.12. PSD particles may contain one or two domains[31], which indicate that the as synthesized FeCo MIs may possess both SD and MD magnetic properties. For MD materials, movement of magnetic domain walls is the main reason for coercivity. While, for SD materials, magnetic domain does not exist and spin flip conversion is the main reason for coercivity. Since the FeCo MIs possess both SD and MD type properties, the coercivity should be higher than those of the Fe_3O_4 and Co MIs (SD material)[32]. As expected, the H_c for the FeCo MIs (49.7 ± 2.2 mT) was higher than the H_c values of the Fe_3O_4 and Co MIs.

Bulk Polymerization of Styrene

The ability of the MIs to initiate free radical polymerization was investigated by monitoring the conversion from the bulk polymerization of styrene. The amount of conversion was compared to that obtained by polymerization with pure azo initiator. Conversion was calculated based off the residual styrene remaining and the use of external standards. In ordered to achieve a useful comparison of the MIs, the grafting densities as obtained by DSC were used to ensure each sample had the same molar concentration of azo initiator. Plot of peak area as a function of concentration for the external standards fitted to a linear regression is shown in supplimentary data Figure A-1. The conversion percent obtained by each MI and that of the pure azo initiator are given in Table 4.

The highest conversion was achieved by the control azo initiator (untethered) followed by the Co, FeCo, and Fe_3O_4 MIs. The MIs produced a lower conversion percentage due to the fact that the azo initiators are anchored to the surface of the particles. This results in clumps of initiator molecules as opposed to a wide distribution of free initiators. If the initiators are too close to one another, produced free radicals may have a difficult time escaping the cage and initiating polymerization due to the steric effects of the surrounding molecules attached to the particle surface, resulting in the recombination of the free radicals[33]. Alternatively, free radicals that escape the cage, initiate polymerization, and become propagating radicals may undergo subsequent radical-radical termination due to the close proximity of other propagating radicals or recently formed radicals near the particle surface[34].

Differences in the conversions achieved by the different MIs can be related to the azo initiator grafting density of the particles. The amount of MI particles present is dependent on the grafting density. Fe_3O_4 has the highest grafting density per particle, and therefore, the number of particles required to obtain the same molar concentration of azo initiator as the other MIs will be less. This can result in a lower distribution of initiator throughout the system, lowering the conversion percentage[33,35] Similarly, the FeCo MIs produce a lower percent conversion than the Co MIs due to higher grafting density.

Table 4: Percent conversion of bulk polymerized styrene initiated by the different MIs and pure azo initiator

Initiator	**Conversion (%)**
Pure Azo initiator	92.3 ± 2.3
Fe_3O_4 MI	72.9 ± 4.3
FeCo MI	77. 5 ± 5.6
Co MI	83.4 ± 1.7

MD simulation

An MD simulation was performed to determine the minimum externally applied force required to break the C─N bond of the azo group. Multiple forces were applied and the C─N bond length was monitored. Once the C─N bond length reached $D_{max,}$ 2.031 Å[16], the bond was considered to be broken. Figure 12 shows the elongation of the C-N bond during the simulation followed by breakage of the bond, Figure 13. Maximum bond lengths achieved for select applied forces are shown in Table 5. From the MD simulation

it was determined that the minimum externally applied force required to break C-N bond of the azo group was 62 ± 1 kcal/mol·Å.

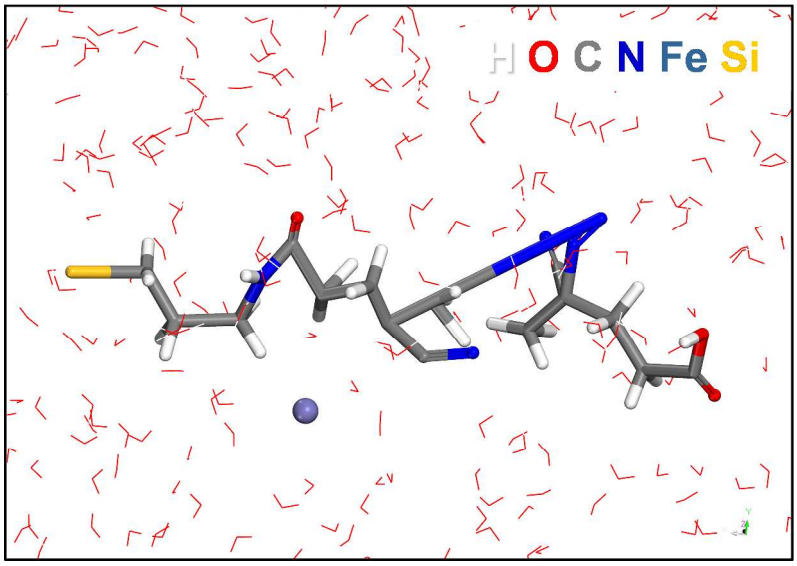

Figure 12. Elongation of C-N bond in APTS-AZO molecule during MD simulation

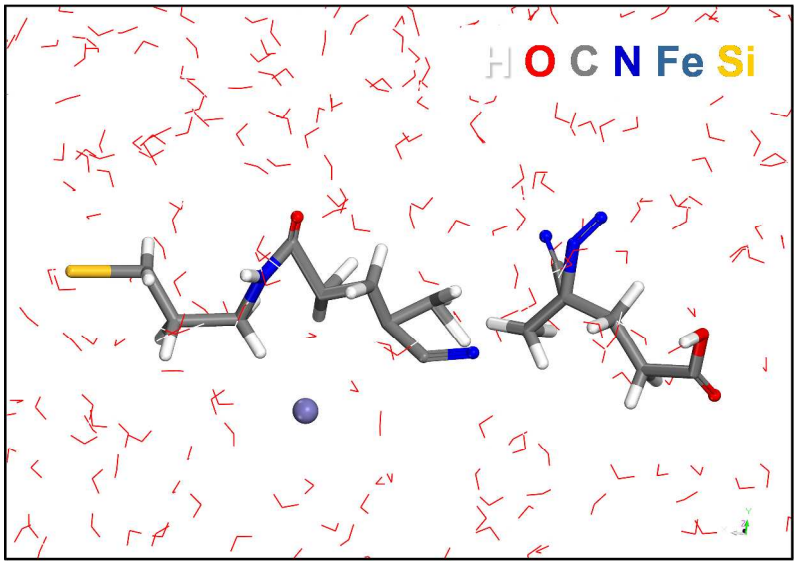

Figure 13. Breakage of C-N bond in APTS-AZO molecule during MD simulation

Table 5. Values of applied force on the Si atom during MD simulations and corresponding maximum stretchable bond length

Applied Force, kcal/mol-Å	Max. bond length (C─N), Å
40	1.75
45	1.79
50	1.82
55	1.85
60	1.89
62	> 2.031 (bond broken)
63	> 2.031
65	> 2.031
68	> 2.031
70	> 2.031

Azoalkanes (RN=NR') dissociate into two alkyl radicals and an N_2 molecule. Evidence for the decomposition of azo compounds suggests that the reaction proceeds through a stepwise mechanism[18,36] as opposed to a concerted one. Due to the fact that this is a stepwise decomposition, only the C-N bond of azo group closest to the magnetic core was monitored for cleavage. This ensures that the calculated force needed to decompose the azo group will be at minimum since, due to energy dissipation, more energy would be needed to break bonds that are farther from the point of applied force. The stepwise mechanism for the decomposition of the MI, grafted azo compound on a magnetic particle, is shown in Scheme 5.

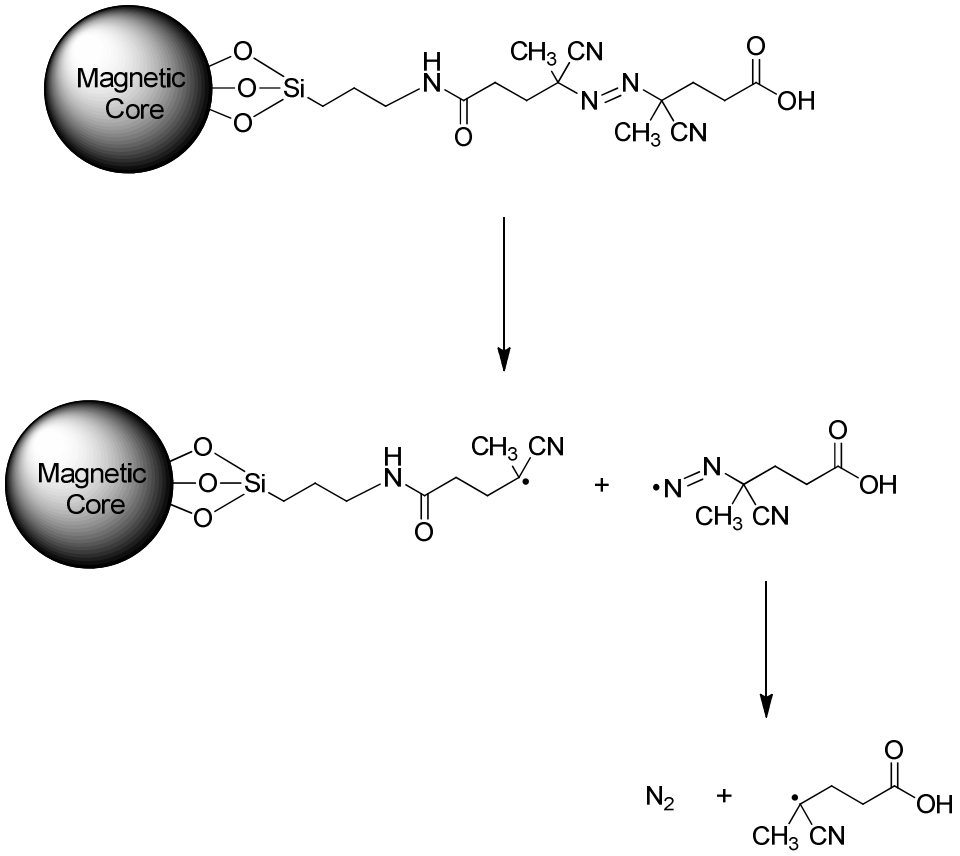

Scheme 5. Stepwise decomposition of MI

Upon application of a force to the magnetic MI, energy will be transfer through the grafted molecule to the weak link. Once enough energy has been transferred, the weak link will break. By modeling the grafted molecule from anchor point to weak link as a spring, Hooke's law ($F = -kx$) can be used to determine the spring constant, k. Figure 14 shows a depiction of the grafted initiator molecule as a spring. Assuming that all other bonds comprising the molecule have negligible change in bond length as compared to the weak C-N bond, k can be calculated by setting x equal to the

displacement of the bond ($D_{max} - r_o$) and F to 62 kcal/mol·Å. Substitution of these into Hooke's law gives a spring constant of 111.5 kcal/mol.

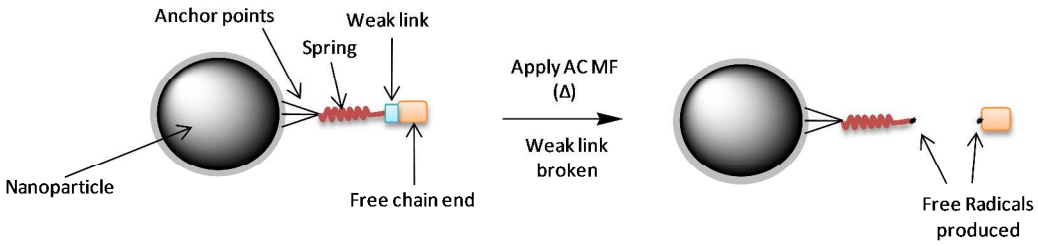

Figure 14: Depiction of grafted intiator as a spring

The Harmonic bond potential of the C-N bond can be given by Equation 8[37],

$$V_B = k(r_{ij} - r_o)^2 \quad (8)$$

where k is the force constant, r_o is the reference bond length (1.474 Å[16]), and r_{ij} is the distance between atoms C and N. Substitution of the value for *k* and r_o into Equation 8 gives the harmonic potential curve shown in Figure 15. Use of D_{max} with Equation 8 results in a C-N bond dissociation energy of 34.5 kcal/mol. The dissociation energy of a C-N bond is reported as 70 kcal/mol[34], which is much higher than that obtained in this study. However, the value of 34.5 kcal/mol corresponds very closely to that of the reported energy of activation, 34 kcal/mol[38], for cleavage of azo C-N bonds and formation of free radicals. The activation energy is much lower that the C-N bond dissociation energy because when the C-N bonds of the azo group contained within the MI break, a very stable N_2 molecule is formed which is energetically favorable[34,39]. Due to closeness of the calculated dissociation energy to that of the reported energy of

activation, it is reasonable to report the minimum force required to break the weak link of the azo group as 62 ± 2 kcal/mol·Å.

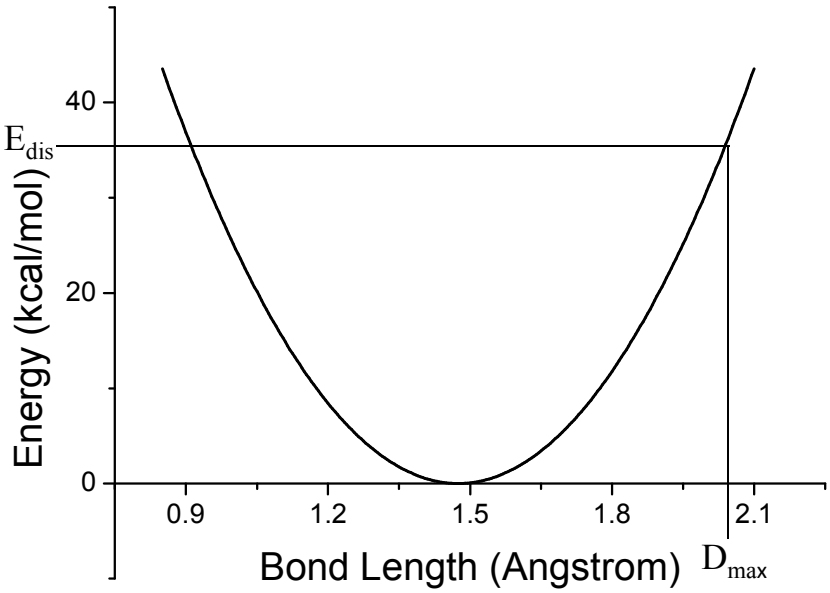

Figure 15. Harmonic potential of C-N bond in azo group

The 62 kcal/mol·Å of force will be applied by means of an AC MF. The magnetic field, H, required to impose the 62 kcal/mol·Å of force onto the magnetic core can be calculated from Equation 9[40]:

$$F_m = \mu_o V_p M_p \cdot \nabla H \tag{9}$$

where F_m is the magnetic force on a particle, μ_o is the permeability of free space, V_p is the volume of the particle, and M_p is the volumetric magnetization of the particle. The volumetric magnetization, M_p, can be given by $M_p = \Delta\chi H$, where $\Delta\chi = \chi_p - \chi_s$; χ_p is the volume magnetic susceptibility of the magnetic particle and χ_s is the volume magnetic

susceptibility of the surrounding medium. Substituting $\Delta\chi H$ for M_p and neglecting χ_s due to its negligible value as compared to χ_p, Equation 9 gives Equation 10.

$$F_m = \mu_o V_p \chi_p H \cdot \nabla H \quad (10)$$

Using Equation 10 in combination with the obtained minimum force of 62 kcal/mol·Å, the minimum magnetic field strength required to break the C-N bond of the azo group can be calculated for each of the MIs. Table 6 lists the calculated magnetic field strength (H) for each of the MIs. The volume of each particle was calculated by averaging the obtained particle diameters from DLS and SEM. The volumetric susceptibility, χ_p, was calculated by multiplying the mass susceptibility χ by the density of the magnetic cores (ρ = 5.18 x 10^3, 4907, and 8900 kg·m^{-3} for Fe_3O_4[41], FeCo[42], and Co[43] respectively).

Table 6. Calculated magnetic field strength required to break the C-N bond for each type of MI

Magnetic Initiator	H (kA/m)
Fe_3O_4	11.15
FeCo	10.01
Co	5.56

According to Equation 10 any applied H above that listed in Table 6 will provide enough force to the MI core to make it possible for the azo group to decompose into free radicals. However, high field strengths and frequencies can result in harmful physiological responses[22b]. Therefore, the operating region of the electromagnet should be chosen such

that the product H*f* is below the threshold value of 4.85 x 10^8 kA m^{-1} s^{-1} allowable for humans[22b,44].

A final experiment was performed as a proof of concept. An *in situ* calorimeter was used to monitor the heat generation of the grafted initiator within an oscillating magnetic field as shown in Figure 16. Control experiments (within an oscillating magnetic field) have been performed for the ungrafted initiator that shows initiation in ~120 °C range similarly to the DSC results. In comparison to the thermal (DSC) and control, exotherms are clearly observed between 30-40 °C. These exotherm temperatures are in accord with the magnetic susceptibility of the magnetic nanoparticles with cobalt having the lowest temperature (exotherm) followed by cobalt-iron, and then iron. Since the heat generated from the magnetic particles (without grafting or initiator present) was subtracted out, this precludes any exotherm derived from the magnetic particles alone. Also, the control experiment precludes any catalytic effect that the magnetic particles may have on the initiator. The only reasonable explanation left is that a chemical reaction has occurred. Although calorimetry alone cannot proof the type of reaction, it is reasonable to assume via bond energies and the modeling that this reaction must be the lowest bond energy which the azo decomposition into a free radical initiator.

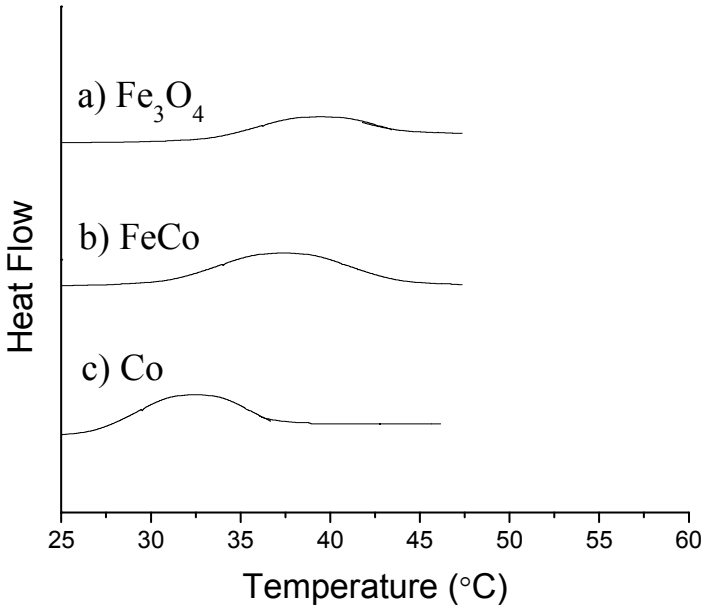

Figure 16: Calorimetic Heat Flow of Magnetic Nanoparticles Grafted with Azo-initiator within an Oscillating Magnetic Field

The new concept of this study is to introduce a new initiation method that will allow polymeric systems to be polymerized without the use of heat or application of radiation as shown in Scheme 5. New magnetic azo-functionalized initiators were prepared and characterized. Through a thermal method, the azo groups were shown to polymerize styrene establishing that the chemical groups to initiate polymerization were located on the magnetic nanoparticle. Through MD simulations, it was shown that with the size and magnetic susceptibility of the particles, an externally applied oscillatory frequency magnetic field can result is hemolytic cleavage of the azo-bond leading to free

radical polymerization. In effect, this would introduce a new cure-on-command technology to the areas of coatings, adhesives, and composites without the line-of-sight issues the photocuring is limited by.

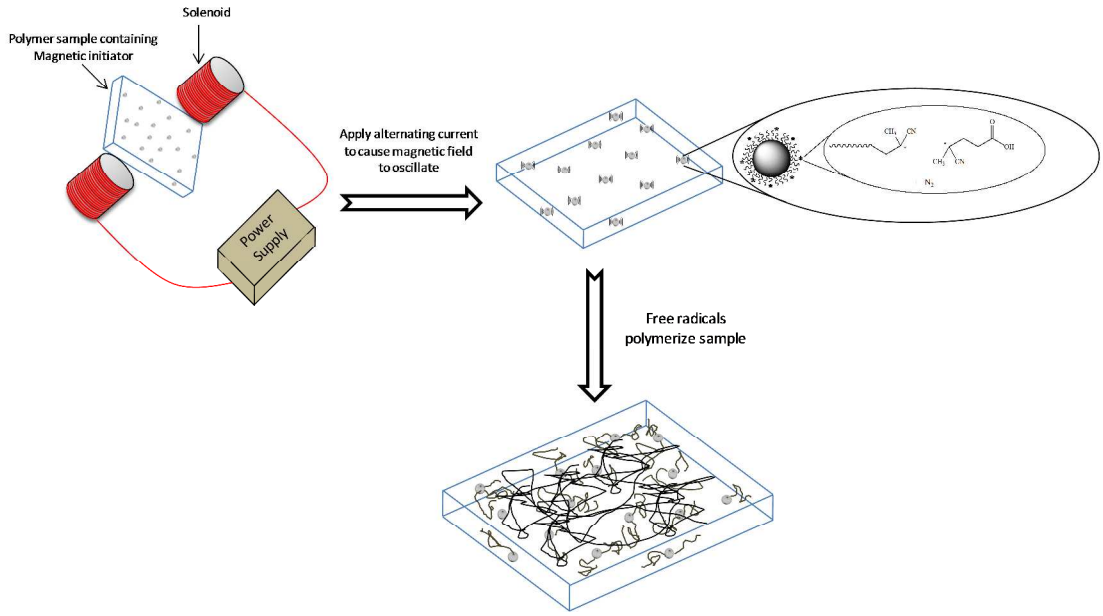

Scheme 6. Curing process of magnetic initiator

Conclusion

Magnetic macro-initiators were synthesized by coating magnetic cores with APTS followed by grafting on an azo-initiator (ACV). Grafting of the azo-initiator was confirmed by FTIR, DSC, and TGA for all magnetic cores, Fe_3O_4, FeCo, and Co. Due to the use of different magnetic cores, it was possible to produce MIs that have the same functional group but possess different magnetic properties. All the MIs were shown to be capable of initiating free radical polymerization, and, as such the MIs can easily be functionalized or incorporated into a polymer matrix. To provide an alternative initiation

method, magnetically induced polymerization via the decomposition of a magnetic macro-initiator under the influence of an externally applied AC MF was shown to be possible through the use of MD simulations. A minimum force of 62 kcal/mol·Å applied to the core of the MI is required in order to decompose the C-N bond of the azo group, producing free radicals.

References

1. Klabunde, K. J., *Nanoscale materials in chemistry*. Wiley-Interscience: New York, 2001; p xi, 292 p.
2. Lewin, M.; Carlesso, N.; Tung, C.-H.; Tang, X.-W.; Cory, D.; Scadden, D. T.; Weissleder, R., Tat peptide-derivatized magnetic nanoparticles allow in vivo tracking and recovery of progenitor cells. *Nat Biotech* **2000,** *18* (4), 410-414.
3. Jeyaprakash, J. D.; Samuel, S.; Dhamodharan, R.; Rühe, J., Polymer Brushes via ATRP: Role of Activator and Deactivator in the Surface-Initiated ATRP of Styrene on Planar Substrates. *Macromolecular Rapid Communications* **2002,** *23* (4), 277-281.
4. Häfeli, U. O., Magnetically modulated therapeutic systems. *International Journal of Pharmaceutics* **2004,** *277* (1–2), 19-24.
5. Xiang, J.-J.; Tang, J.-Q.; Zhu, S.-G.; Nie, X.-M.; Lu, H.-B.; Shen, S.-R.; Li, X.-L.; Tang, K.; Zhou, M.; Li, G.-Y., IONP-PLL: a novel non-viral vector for efficient gene delivery. *The Journal of Gene Medicine* **2003,** *5* (9), 803-817.
6. Torchilin, V. P., Drug targeting. *European Journal of Pharmaceutical Sciences* **2000,** *11, Supplement 2* (0), S81-S91.
7. Babu, K.; Dhamodharan, R., Grafting of Poly(methyl methacrylate) Brushes from Magnetite Nanoparticles Using a Phosphonic Acid Based Initiator by Ambient Temperature Atom Transfer Radical Polymerization (ATATRP). *Nanoscale Research Letters* **2008,** *3* (3), 109-117.
8. Garcia, I.; Zafeiropoulos, N. E.; Janke, A.; Tercjak, A.; Eceiza, A.; Stamm, M.; Mondragon, I., Functionalization of iron oxide magnetic nanoparticles with poly(methyl methacrylate) brushes via grafting-from atom transfer radical polymerization. *Journal of Polymer Science Part A: Polymer Chemistry* **2007,** *45* (5), 925-932.
9. Matsuno, R.; Yamamoto, K.; Otsuka, H.; Takahara, A., Polystyrene- and Poly(3-vinylpyridine)-Grafted Magnetite Nanoparticles Prepared through Surface-Initiated Nitroxide-Mediated Radical Polymerization. *Macromolecules* **2004,** *37* (6), 2203-2209.
10. Wang, Y.; Teng, X.; Wang, J.-S.; Yang, H., Solvent-Free Atom Transfer Radical Polymerization in the Synthesis of Fe2O3@Polystyrene Core−Shell Nanoparticles. *Nano Letters* **2003,** *3* (6), 789-793.
11. Hayashi, S.; Takeuchi, Y.; Eguchi, M.; Iida, T.; Tsubokawa, N., Graft polymerization of vinyl monomers initiated by peroxycarbonate groups introduced onto silica surface by Michael addition. *Journal of Applied Polymer Science* **1999,** *71* (9), 1491-1497.
12. (a) Hartmann, P. C.; Sanderson, R. D., Preparation of Magnetite-Polystyrene Core-Shell Hybrid Nanoparticles, Initiated by a Covalently Bonded Azo Compound. *Macromolecular*

Symposia **2007,** *255* (1), 24-35; (b) Tsubokawa, N.; Kogure, A.; Maruyama, K.; Sone, Y.; Shimomura, M., Graft polymerization of vinyl monomers from inorganic ultrafine particles initiated by azo groups introduced onto the surface. *Polym. J. (Tokyo)* **1990,** *22*, 827-33.

13. (a) Horák, D.; Shagotova, T.; Mitina, N.; Trchová, M.; Boiko, N.; Babič, M.; Stoika, R.; Kovářová, J.; Hevus, O.; Beneš, M. J.; Klyuchivska, O.; Holler, P.; Zaichenko, A., Surface-Initiated Polymerization of 2-Hydroxyethyl Methacrylate from Heterotelechelic Oligoperoxide-Coated γ-Fe_2O_3 Nanoparticles and their Engulfment by Mammalian Cells. *Chemistry of Materials* **2011,** *23* (10), 2637-2649; (b) Babu, K.; Dhamodharan, R., Synthesis of Polymer Grafted Magnetite Nanoparticle with the Highest Grafting Density via Controlled Radical Polymerization. *Nanoscale Research Letters* **2009,** *4* (9), 1090 - 1102; (c) Li, X.; Sun, Z., Synthesis of magnetic polymer microspheres and application for immobilization of proteinase of balillus sublitis. *Journal of Applied Polymer Science* **1995,** *58* (11), 1991-1997. d) Li, B.; Yu, B.; Ye, Q.; Zhou, Feng; Tapping the potential of polymer brushes through synthesis , Acc. Chem. Res,. 2015, 48 (2), 229-237. e) Liu, G.; Cai, M.; Wang, X; Zhou, F.; Liu, W. Core-Shell-Corona Structured Polyelectrolyte brushes-grafting Magnetic nanoparticles for water harvesting ACS Appl Mater Interfaces, 2014, 6(14): 11625-11632.
14. Kroell, M.; Zimmermann, G., Bonding and Debonding on Command. **2004**.
15. Engel, T.; Reid, P *Thermodynamics, statistical thermodynamics, & kinetics*, 2nd ed., Prentiss Hall, 2010.
16. Rosensweig, R.E. Heating magnetic fluid with alternating magnetic field. J. Magn. Mater. **2002**, 252, 370-4.
17. Heinz, H., Computational screening of biomolecular adsorption and self-assembly on nanoscale surfaces. *Journal of Computational Chemistry* **2010,** *31* (7), 1564-1568.
18. Hu, C.-H.; Schaefer, H. F., III, The Mechanism of the Thermal Decomposition and the (n-.pi.*) Excited States of Azomethane. *The Journal of Physical Chemistry* **1995,** *99* (19), 7507-7513.
19. Sun, C.; Lee, J. S. H.; Zhang, M., Magnetic nanoparticles in MR imaging and drug delivery. *Advanced Drug Delivery Reviews* **2008,** *60* (11), 1252-1265.
20. (a) Prucker, O.; Rühe, J., Synthesis of Poly(styrene) Monolayers Attached to High Surface Area Silica Gels through Self-Assembled Monolayers of Azo Initiators. *Macromolecules* **1998,** *31* (3), 592-601; (b) Parvole, J.; Montfort, J.-P.; Billon, L., Formation of Inorganic/Organic Nanocomposites by Nitroxide-Mediated Polymerization in Bulk Using a Bimolecular System. *Macromolecular Chemistry and Physics* **2004,** *205* (10), 1369-1378.
21. (a) Gubin, S. P., *Magnetic nanoparticles*. Wiley-VCH: Weinheim, 2009; p xiv, 466 p; (b) Thanh, N. T. K., *Magnetic nanoparticles : from fabrication to clinical applications*. Taylor & Francis: Boca Raton, 2012.
22. (a) Tartaj, P.; Morales, M. d. P.; Veintemillas-Verdaguer, S.; Gonzalez-Carreno, T.; Serna, C. J., The preparation of magnetic nanoparticles for applications in biomedicine. *J. Phys. D: Appl. Phys.* **2003,** *36*, R182-R197; (b) Pankhurst, Q. A.; Connolly, J.; Jones, S. K.; Dobson, J., Applications of magnetic nanoparticles in biomedicine. *Journal of Physics D: Applied Physics* **2003,** (13), R167.
23. Kumar, C. S. S. R., *Magnetic nanomaterials*. Wiley-VCH: Weinheim, Germany, 2009; p xxiv, 648 p.

24. Chen, F.; Xue, Y.; Hadjiev, V. G.; Chu, C. W.; Nikolaev, P.; Arepalli, S., Fast characterization of magnetic impurities in single-walled carbon nanotubes. *Applied Physics Letters* **2003,** *83* (22), 4601-4603.
25. Nikitenko, S. I.; Koltypin, Y.; Palchik, O.; Felner, I.; Xu, X. N.; Gedanken, A., Synthesis of Highly Magnetic, Air-Stable Iron–Iron Carbide Nanocrystalline Particles by Using Power Ultrasound. *Angewandte Chemie International Edition* **2001,** *40* (23), 4447-4449.
26. Wu, P.-C.; Wang, W.-S.; Huang, Y.-T.; Sheu, H.-S.; Lo, Y.-W.; Tsai, T.-L.; Shieh, D.-B.; Yeh, C.-S., Porous Iron Oxide Based Nanorods Developed as Delivery Nanocapsules. *Chemistry – A European Journal* **2007,** *13* (14), 3878-3885.
27. Mohapatra, S.; Pramanik, N.; Mukherjee, S.; Ghosh, S.; Pramanik, P., A simple synthesis of amine-derivatised superparamagnetic iron oxide nanoparticles for bioapplications. *Journal of Materials Science* **2007,** *42* (17), 7566-7574.
28. Kuhrt, C.; Schultz, L., Formation and magnetic properties of nanocrystalline mechanically alloyed Fe-Co. *Journal of Applied Physics* **1992,** *71* (4), 1896-1900.
29. Hesani, M.; Yazdani, A.; Abedi Ravan, B.; Ghazanfari, M., The effect of particle size on the characteristics of FeCo nanoparticles. *Solid State Communications* **2010,** *150* (13–14), 594-597.
30. Dunlop, D. J., Temperature, time and interaction effects in rock magnetism. *J. Magn. Magn. Mater.* **1984,** *45*, 107-12.
31. Zhao, Y.; Dunnill, C. W.; Zhu, Y.; Gregory, D. H.; Kockenberger, W.; Li, Y.; Hu, W.; Ahmad, I.; McCartney, D. G., Low-Temperature Magnetic Properties of Hematite Nanorods. *Chemistry of Materials* **2007,** *19* (4), 916-921.
32. Lv, B.; Xu, Y.; Wu, D.; Sun, Y., Preparation and magnetic properties of spindle porous iron nanoparticles. *Materials Research Bulletin* **2009,** *44* (5), 961-965.
33. Denisov, E. T.; Denisova, T. G.; Pokidova, T. S., *Handbook of free radical initiators*. Wiley-Interscience: Hoboken, N.J., 2003; p xxii, 879 p.
34. Odian, G. G., *Principles of polymerization*. 4th ed.; Wiley-Interscience: Hoboken, N.J., 2004; p xxiv, 812 p.
35. Kricheldorf, H. R.; Nuyken, O.; Swift, G., *Handbook of polymer synthesis*. 2nd ed.; Marcel Dekker: New York, 2005; p viii, 965 p.
36. (a) Dannenberg, J. J.; Rocklin, D., A theoretical study of the mechanism of the thermal decomposition of azoalkanes and 1,1-diazenes. *The Journal of Organic Chemistry* **1982,** *47* (23), 4529-4534; (b) Engel, P. S.; Gerth, D. B., Thermolysis of acyclic azoalkanes: simultaneous or stepwise carbon-nitrogen homolysis? *Journal of the American Chemical Society* **1983,** *105* (23), 6849-6851; (c) Lazár, M., *Free radicals in chemistry and biology*. CRC Press: Boca Raton, Fla., 1989; p 304 p.
37. PumMa, M. D. P. Theory: Potentials. http://www.pumma.nl/index.php/Theory/Potentials.
38. The property of the Azo polymerization initiator. http://www.otsukac.co.jp/en/products/chemical/azo/ (accessed January 5).
39. Mishra, M. K.; Yagci, Y., *Handbook of vinyl polymers : radical polymerization, process, and technology*. 2nd ed.; CRC Press/Taylor & Francis: Boca Raton, 2009; p 763 p.
40. (a) Gerber, R.; Birss, R. R., *Magnetic Materials and Their Applications Series, Vol. 1: High Gradient Magnetic Separation*. Research Studies Press: 1983; p 209 pp; (b) Moeser, G. D.; Roach, K. A.; Green, W. H.; Alan Hatton, T.; Laibinis, P. E., High-gradient magnetic separation of coated magnetic nanoparticles. *AIChE Journal* **2004,** *50* (11), 2835-2848.
41. Zhao, Y.; Xu, Z.; Parhizkar, M.; Fang, J.; Wang, X.; Lin, T., Magnetic liquid marbles, their manipulation and application in optical probing. *Microfluidics and Nanofluidics*, 1-10.

42. Sawyer, C. A.; Habib, A. H.; Miller, K.; Collier, K. N.; Ondeck, C. L.; McHenry, M. E., Modeling of temperature profile during magnetic thermotherapy for cancer treatment. *Journal of Applied Physics* **2009,** *105* (7), 07B320.
43. Davis, J. R.; ASM International. Handbook Committee., *Nickel, cobalt, and their alloys*. ASM International: Materials Park, OH, 2000; p 442 p.
45. Atkinson, W. J.; Brezovich, I. A.; Chakraborty, D. P., Usable Frequencies in Hyperthermia with Thermal Seeds. *Biomedical Engineering, IEEE Transactions on* **1984,** *BME-31* (1), 70-75.

Appendix

Table A-1. Force field parameters for APTS-AZO initiator, data refer to PCFF force field

Element (Force Field Type)	Charge (*e*)	r_0 (pm)	E_0 (kcal/mol)
Si (si)	+0.135	4.45	0.190
C^1 (c2)	–0.241	4.01	0.054
C^2 (c2)	–0.106	4.01	0.054
C^3 (c2)	0.104	4.01	0.054
C^4 (c_1)	0.427	3.81	0.120
C^5 (c)	0.340	4.01	0.054
C^6 (c_1)	0.500	3.81	0.120
C^7 (c3)	–0.159	4.01	0.054
C^8 (ct)	0.080	4.01	0.064
N (n2)	–0.699	4.07	0.106
N (n=)	–0.300	3.80	0.080

N (nt)	–0.200	3.57	0.065
O (o_1)	–0.531	3.30	0.267
O (o_2)	–0.594	3.42	0.240
H (hc)	0.053	2.99	0.020
H (hn2)	0.378	1.65	0.013
H (ho2)	0.300	1.11	0.013
Fe (Fe)	0.700	2.66	13.889
II. Bonds		r_0 (pm)	k_r [kcal/(mol-Å^2)] k_2 (k_3) [k_4]
Si–C (Si – c2)		1.89	189.65 (–279.42) [307.51]
C–C (c2 – c2)		1.53	299.67 (–501.77) [679.81]
C–N (c2 – n2)		1.46	319.15 (–586.32) [961.41]
N–C (n2 – c_1)		1.36	390.67 (–768.37) [923.24]
C–C (c_1 – c2)		1.52	253.70 (–423.03) [396.90]
C–C (c2 – c)		1.53	299.67 (–501.77) [679.81]
C–N (c – n=)		1.47	336 (0) [0]
N=N (n= – n=)		1.21	651.2 (0) [0]
N–C (n= – c)		1.47	336 (0) [0]
C–C (c – c2)		1.53	299.67 (–501.77) [679.81]
C–C (c2 – c_1)		1.52	253.70 (–423.03) [396.90]
C–C (c – ct)		1.42	340 (0) [0]
C–N (ct – nt)		1.15	880 (0) [0]
C–C (c – c3)		1.53	299.67 (–501.77) [679.81]
C–O (c_1 – o_1)		1.20	851.14 (–1918.48) [2160.76]

C–O (c_1 – o_2)	1.36	367.14 (–794.79) [1055.23]
C–H (c – hc)	1.10	345 (–691.89) [844.6]
C–H (c3 – hc)	1.10	345 (–691.89) [844.6]
O–H (o_2 – ho2)	0.95	534.29 (–1287.19) [1889.13]
III. Angle	θ_0 (deg)	k_θ [kcal/(mol-rad^2)] k_2 (k_3) [k_4]
Si–C–C (Si – c2 – c2)	112.67	39.51 (–7.44) [0]
C–C–C (c2 – c2 – c2)	112.67	39.51 (–7.44) [–9.55]
C–C–N (c2 – c2 – n2)	109.83	76.89 (–48.73) [18.01]
C–N–C (c2 – n2 – c_1)	122.70	60.46 (–29.61) [0]
N–C–C (n2 – c_1 – c2)	116.92	29.41 (–10.99) [–8.77]
C–C–C (c_1 – c2 – c2)	108.52	51.97 (–9.48) [–10.99]
C–C–C (c2 – c2 – c)	112.67	39.51 (–7.44) [–9.55]
C–C–N (c2 – c – n=)	117.28	55.44 (0) [0]
C–N–N (c – n= – n=)	112.67	39.51 (–7.44) [–9.55]
N–N–C (n= – n= – c)	112.67	39.51 (–7.44) [–9.55]
N–C–C (n= – c – c2)	117.28	55.44 (0) [0]
C–C–C (c – c2 – c2)	112.67	39.51 (–7.44) [–9.55]
C–C–C (c2 – c2 – c_1)	108.52	51.97 (–9.48) [–10.99]

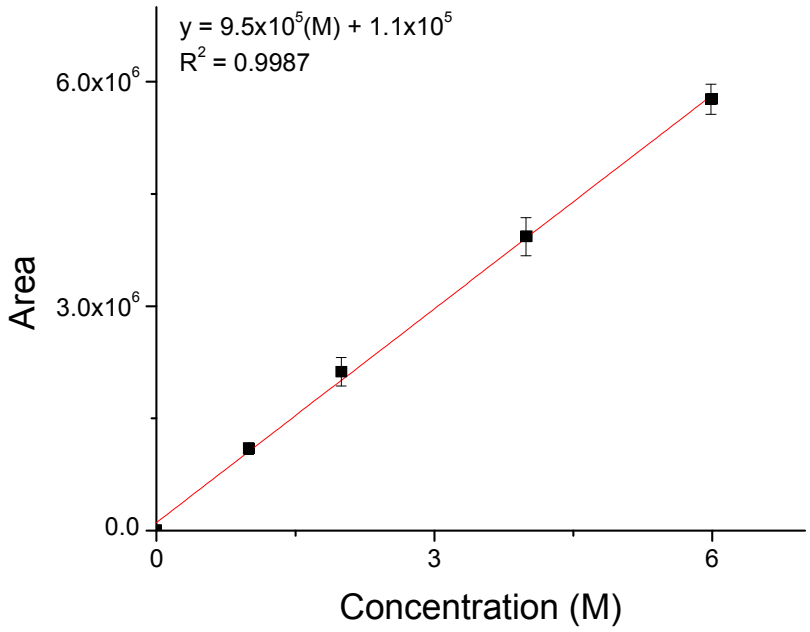

Figure A-1: Detector Response Ratio of styrene concentration using GC

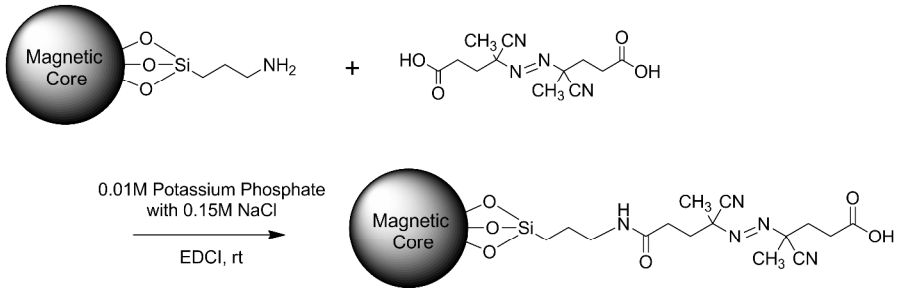

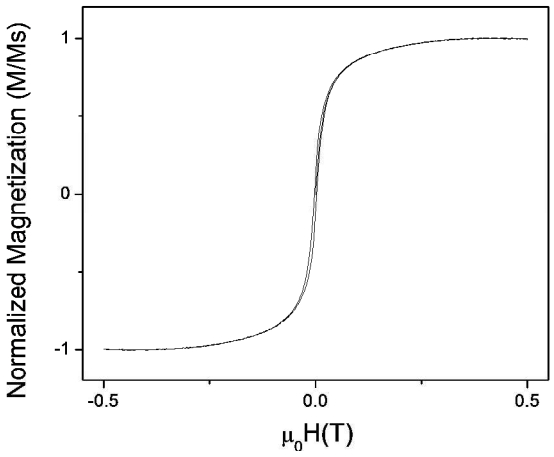

Hysteresis curve for Co macro-initiator

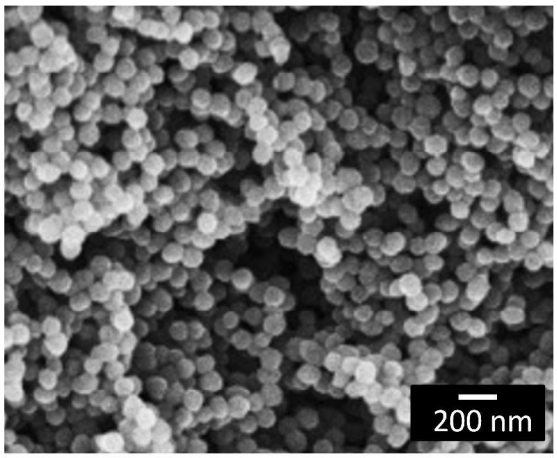

SEM image for Co macro-initiator